A tug of war between filament treadmilling and myosin induced contractility generates actin cortex — Source link ↗

Qin Ni, Kaustubh Wagh, Arpita Upadhyaya, Garegin A. Papoian

Institutions: University of Maryland, College Park

Topics: Treadmilling, Podosome, Myosin and Actin

Related papers:

- Turnover versus treadmilling in actin network assembly and remodeling.

- Myosin-driven actin-microtubule networks exhibit self-organized contractile dynamics

- The non-processive rice kinesin-14 OsKCH1 transports actin filaments along microtubules with two distinct velocities.

- The dynamics of actin network turnover is self-organized by a growth-depletion feedback.

- Bundling actin filaments from membranes: some novel players

Share this paper: 🅕 🅣 in ✉

View more about this paper here: https://typeset.io/papers/a-tug-of-war-between-filament-treadmilling-and-myosin-1h2od13aio

A tug of war between filament treadmilling and myosin induced contractility generates actin cortex

Qin Ni
University of Maryland, College Park

Kaustubh Wagh
University of Maryland, College Park   https://orcid.org/0000-0001-8514-027X

Arpita Upadhyaya
University of Maryland College Park

Garegin Papoian (✉ gpapoian@umd.edu)
University of Maryland, College Park

Article

A tug of war between filament treadmilling and myosin induced contractility generates actin cortex

Qin Ni,[1] Kaustubh Wagh,[2] Arpita Upadhyaya,[2,3*] Garegin A. Papoian,[2,4*]

[1]Department of Chemical and Biomolecular Engineering
[2]Department of Physics
[3]Institute for Physical Science and Technology
[4]Department of Chemistry and Biochemistry
University of Maryland, College Park, MD, USA

[*]To whom correspondence should be addressed; E-mail: arpitau@umd.edu; gpapoian@umd.edu.

In most eukaryotic cells, actin filaments assemble into a shell-like actin cortex under the plasma membrane, controlling cellular morphology, mechanics, and signaling. The actin cortex is highly polymorphic, adopting diverse forms such as the ring-like structures found in podosomes, axonal rings, and immune synapses. The biophysical principles that underlie the formation of actin cortices and their structural plasticity remain unknown. Using a molecular simulation platform, called MEDYAN, we discovered that varying the filament treadmilling rate induces a finite size phase transition in actomyosin network structure. We found that actomyosin networks condense into clusters at low treadmilling rates but form ring-like or cortex-like structures at high treadmilling rates. This mechanism is supported by our corroborating experiments on live T cells, which show that disrupting filament treadmilling induces centripetal collapse of pre-existing actin rings and the formation of clusters. Our

analyses suggest that the actin cortex is a preferred state of low mechanical energy, which is, importantly, only reachable at high treadmilling rates.

Main Text

A shell-like cortex, primarily comprised of actin and myosin, is ubiquitously found under the cell membrane of eukaryotic cells. The cortex is characterized by a mesh-like geometry, and plays an indispensable role in defining cellular shape and mechanochemical responses (*1–4*). Actin filaments within the cortex are highly dynamic, undergoing rapid polymerization and depolymerization, and are subject to contractile forces from myosin motors (*5, 6*). Actin polymerization is polarized: monomeric actin (G-actin) binds to the barbed ends of filaments and polymeric actin (F-actin) dissociates from the pointed ends in a process called treadmilling (*7–9*). As a result, the actin cortex is a dynamically polymorphic structure that is capable of rapid remodeling in response to biochemical signals and physical stimuli (*10, 11*). Actin cortices can adopt a diversity of shapes. For instance, in immune cells such as T cells, the actin cortex reorganizes into a quasi-2D actin ring that sequesters different signaling complexes in separate concentric domains upon stimulation by an antigen-presenting cell (*12–16*). Ring-like actin geometries have also been widely found in other sub-cellular structures such as podosomes and axons (*17, 18*). Despite their importance, the fundamental physical mechanisms underlying the formation of these structures are still not well understood.

In notable contrast to the shell-like or ring-like networks ubiquitously seen in living cells, *in vitro* experiments primarily produce actomyosin networks comprised of clusters that originate from global geometric collapse due to myosin motor driven contractility (*10, 19–23*). We hypothesized that this apparent disparity between the predominant actomyosin architectures formed *in vitro* versus those observed *in vivo* may arise from the large difference in the corresponding treadmilling rates: *in vitro* networks reconstituted from purified proteins exhibit

2

treadmilling rates that are often several-fold slower than those observed *in vivo* due to the lack of actin filament polymerization and disassembly promoters (*24–28*). A systematic way to explore how the treadmilling rate affects actomyosin network architecture is essential to probe this hypothesis. This is a difficult experimental task, requiring careful manipulation of molecular machinery and actin polymerization kinetics. Such limitations can be overcome by computer simulations, which provide a powerful way to capture the complex chemistry and mechanics of the active cytoskeleton, and bring significant mechanistic insights.

In order to find a minimal set of conditions that lead to the formation of rings and cortices, we used the open-access simulation platform MEDYAN (*21*) (Mechanochemical Dynamics of Active Networks) to model contractile actomyosin networks. We find that the competition between actin filament treadmilling and myosin contractility determines the overall network morphology. Our simulations showed that the speed of actin filament treadmilling drives the network away from global centripetal actomyosin clustering, resulting in centrifugal condensation that creates ring-like and cortex-like structures, without tethering filaments to the boundary. Our corroborating experiments on live T cells showed that, indeed, inhibiting filament treadmilling via Latrunculin A (LatA) disassembled pre-existing actin rings, causing the network to condense centripetally and creating small clusters. Furthermore, our computational analysis indicates that actin filaments located at the network periphery have lower mechanical energy as compared to those forming actomyosin clusters and hence represent the energetically preferred configuration. However, this energetic state is only achievable at high treadmilling rates, while at lower treadmilling rates, the system gets trapped in long-lived metastable states where actin filaments instead condense into clusters. In summary, our work shows that a tug of war between filament treadmilling and myosin-induced contraction determines the fate of actomyosin architectures: the energetically favorable cortex/ring states are kinetically accessible only at higher treadmilling rates. Our findings reveal that the assembly and stability of various cellular

3

actin structures are crucially regulated by the fine-tuning of filament treadmilling, which can be achieved by the activation of accessory proteins, such as formin, profilin, and cofilin, via local biochemical signaling.

We used MEDYAN simulations to probe the mechanisms underlying the formation of actin cortices and rings. MEDYAN couples sophisticated, single molecule level treatment of cytoskeletal reactions, polymer mechanics, and mechanochemical feedback to model complex actomyosin networks. Actin networks were simulated in a thin oblate cylinder at diameters between 3.8 μm and 10 μm, to mimic the lateral dimension of small human cells. Model details can be found in Methods and Supplementary Information Section-1 (SI-1). We first modeled networks in the absence of non-muscle myosin II (NMII) and alpha-actinin crosslinkers at different average treadmilling rates ($\langle r_{TM} \rangle$ = 0.57 s^{-1}, 1.41 s^{-1}, and 2.21 s^{-1}) based on actin filament assembly kinetics reported from prior experiments (*24, 29, 30*). These systems also include a filament nucleator, formin, at a concentration of 100 nM (*9, 31*). We found that disordered actin networks were created at all treadmilling conditions tested (Fig. S1b). We quantified the spatiotemporal evolution of the network geometry by plotting the median of the radial filament density distribution (R_{median}) as a function of time (Fig. S1a). In NMII-free networks, we observed a relatively uniform filament density across the network regardless of treadmilling rates (Fig. S1c). In this case, the network geometry is dominated by stochastic filament treadmilling that is not spatially biased. The boundary plays an important role, as the boundary repulsion force inhibits barbed end polymerization such that filaments reaching the boundary rapidly depolymerize and eventually disassemble. The loss of filaments through depolymerization is compensated by the nucleation of new filaments, resulting in dynamic and disordered structures (Video 1).

We next explored how these disordered networks behaved upon the introduction of crosslinking and motor contractility. We allowed the network to evolve for 300 s at different $\langle r_{TM} \rangle$ as de-

scribed above to establish a disordered structure, and then added NMIIs and the actin crosslinker alpha-actinin to generate contractile forces. The addition of NMIIs and crosslinkers changed the steady state network geometry, as measured by R_{median} (Fig. 1a). For slow treadmilling rates ($\langle r_{TM} \rangle = 0.56 s^{-1}$), the addition of NMIIs and alpha-actinin resulted in the clustering of actin filaments (Fig. 1b-iii, and Video 2). The average local concentration of actin within the clusters was 234 μM, which is almost six-fold higher than the initial G-actin concentration (40 μM), suggesting a high degree of geometric localization. This geometric pattern is consistent with prior *in vitro* and *in silico* studies on contractile actomyosin networks (*10, 19, 20, 22*), where contractility can be defined as a symmetry breaking event accompanied by a geometric collapse of the network. Although the size and location of actin clusters varied significantly between duplicated trajectories (Fig. S2), a decreasing R_{median} suggests that the overall collapse is centripetal (Fig. 1b-iii).

Our simulations suggest that actin networks are subject to two competing processes: treadmilling tends to homogeneously distribute filaments in the network, while NMII tends to generate contractility that traps filaments into clusters. We thus explored changes in the actin network geometry by increasing the treadmilling rate while maintaining the same concentration of NMII. Although filament nucleation occurs stochastically throughout the entire network and there is no filament tethering near the boundary, we discovered that after the addition of NMII to rapidly treadmilling networks ($\langle r_{TM} \rangle = 2.05 s^{-1}$), filaments steadily accumulate at the network boundary (Fig. 1a-i, and Video 3). During this process, we observed that NMIIs deformed many filaments and gradually changed their orientation from being perpendicular to the boundary to parallel (Video 4). Upon allowing the system to further evolve for several hundred seconds, we found that actin networks transformed into ring-like structures (Fig. 1b-i). Networks with intermediate $\langle r_{TM} \rangle = 0.94 s^{-1}$ form a mixture of clusters and rings (Fig. 1b-ii, and Video 5).

The resulting actin rings are highly condensed, having a thickness of a few hundred nanome-
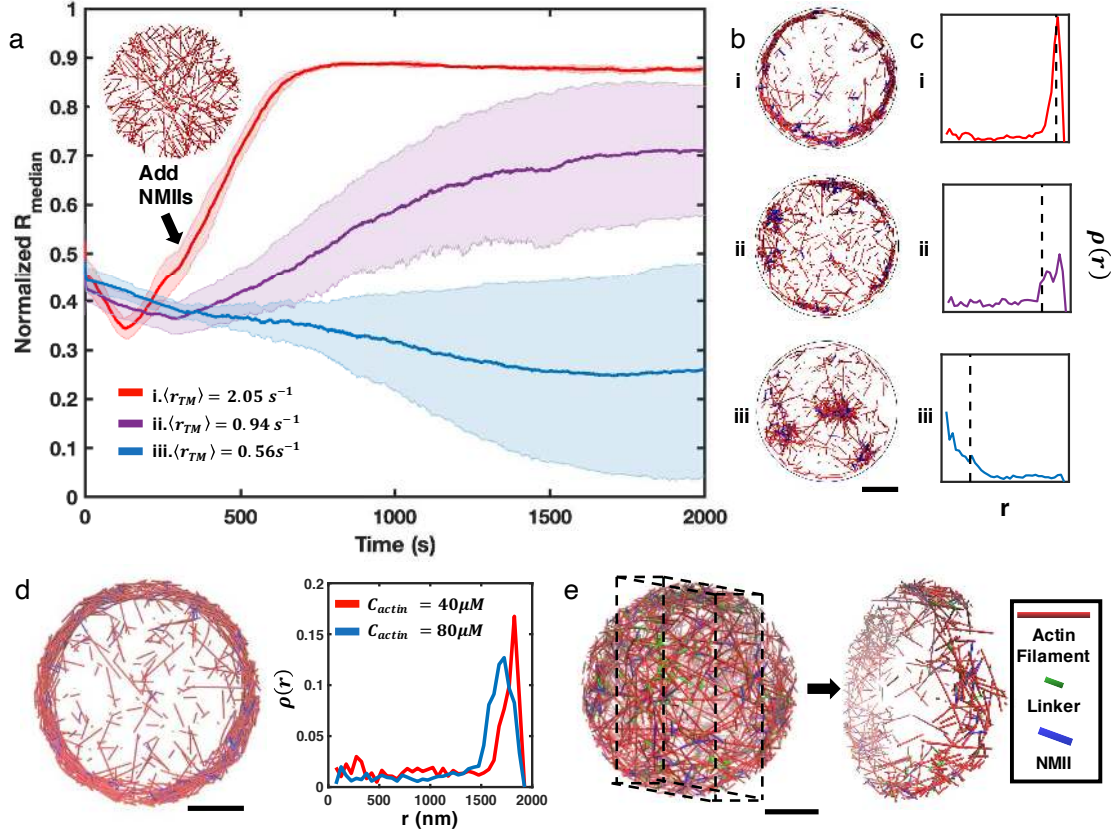
Figure 1: **NMII contractility induces geometric collapse of treadmilling actin filaments.** (a) Normalized medians of radial filament density distribution (R_{median}) at different treadmilling rates ($\langle r_{TM} \rangle$) are shown. The treadmilling rate is defined as the average number of actin monomers added per filament per second at the barbed ends - equivalent to the rate of F-actin depletion from the pointed ends - after reaching the kinetic steady state (SI-2). 0.06 μM of NMII and 4 μM of alpha-actinin were added at 301 s. The inset figure is a snapshot at t = 300 s of networks with $\langle r_{TM} \rangle = 2.05 s^{-1}$. The shaded error bars represent the standard deviation across 5 runs. (b-c) Representative snapshots at each treadmilling condition (b) and their radial filament density distribution, $\rho(r)$ (c) are shown. Dashed lines in (c) indicate the position of R_{median}. (d) Representative snapshot of ring-like networks with 80 μM actin (left), and $\rho(r)$ of actin rings with 40 μM actin and 80 μM actin are shown ($\langle r_{TM} \rangle = 1.35$ s^{-1}). (e) A snapshot of a spherical cortex-like network (left) and a slice showing the internal structure (right). (a,b,d,e) Actin filaments are red cylinders, NMIIs are blue cylinders and linkers are green cylinders in all snapshots. All scale bars are 1 μm.

6

ters and exhibiting local actin concentrations similar to those found in actin clusters (263 µM). Increasing the initial G-actin concentration increases the thickness of actin rings (Fig. 1d). Most filaments in actin rings are oriented parallel to the boundary (Fig. S3), forming small actin clusters that undergo azimuthal flow (Video 3). Analogous ring-like patterns were observed on a larger system with a diameter of 10 µm (Fig. S4). In a spherical system, networks evolved into hollow spherical cortex-like geometries under similar conditions (Fig. 1e, Fig. S5, and Video 6).

In order to further understand how treadmilling regulates ring-like actin networks, we experimentally examined the F-actin dynamics in live Jurkat T cells. Upon activation with stimulatory antibodies, the actin cytoskeleton in T cells reorganizes into a ring-like structure (*12–16*). This consists of an outer lamellipodial region with Arp2/3 generated branched actin filaments undergoing retrograde flows and an inner lamellar ring formed by formin-nucleated linear actin filaments decorated with NMII. We note that our simulations are in qualitative agreement with and intended to model salient aspects of formin-based actomyosin rings. Since it is not feasible to directly control the treadmilling rate in experiments, we used the actin inhibitor, Latrunculin-A (LatA), as a reasonable proxy to achieve a similar effect. LatA is a toxin that decreases the polymerization rate and increases the depolymerization rate by sequestering G-actin and accelerating phosphate release from ADP-Pi-actin (*30, 32, 33*). We used EGFP-F-tractin, an indirect reporter of F-actin to visualize the actin network. EGFP-F-tractin expressing Jurkat T cells were allowed to spread on an activating glass surface coated with anti-CD3 antibody and imaged with time-lapse total internal reflection fluorescence (TIRF) microscopy to visualize the dynamic actin reorganization into a ring (Video 7). Upon formation of the actin ring at the contact zone, LatA (at different concentrations) was added to spreading cells and the resulting effect on the rings was monitored with continuous imaging. In order to compare with simulations, we used the fluorescence intensity as a reporter of F-actin distribution and calculated a normalized R_{median} to quantify the evolution of the actin network under vehicle control (Video 8) and vary-

ing degrees of LatA inhibition. With weak treadmilling inhibition (C_{LatA} =250 nM), the ring like structure is perturbed but largely preserved for several minutes after inhibition (Fig. 2b, and Video 9). At higher doses of LatA (C_{LatA} =500 nM and 1 µM), R_{median} rapidly decreases, indicating a collapse of the network towards the geometric center of the cell (Fig. 2c-d, and Video 10-11). The rate of centripetal collapse of the actin network increases with increasing C_{LatA} (Fig. 2e-f). The dismantling of the actin ring is also accompanied by the formation of F-actin clusters or bundles (Fig. 2b-d).

To compare with experiments, we perturbed $\langle r_{TM} \rangle$ *in silico* to model the effect of LatA after ring-like networks are established. For simplicity, we reduced the polymerization rate constants and increased the depolymerization rate constants. Actin rings were created in the same way as shown in Figure 1a-i for the first 800 seconds of simulation. After 800 seconds, $\langle r_{TM} \rangle$ was reduced to $2.05 s^{-1}$ (no inhibition, Fig. 3a), $1.80 s^{-1}$ (weak inhibition, Fig. 3b), and $0.50 s^{-1}$ (strong inhibition, Fig. 3c) respectively to closely follow the T cell experiments (see SI-2 for more details). We found that actin rings persist with weak treadmilling inhibition (Fig. 3b), while they collapse into clusters under strong inhibition (Fig. 3c). Measurements of R_{median} and the rate of collapse (Fig. 3d-e) at different inhibition conditions demonstrate the centripetal collapse of the ring network, reproducing the above-described experimental observations.

Both our simulations and experimental observations suggest that variation of the treadmilling rate affects the emergence of distinct actomyosin architectures. To further probe this hypothesis, we performed extensive computer simulations at different treadmilling rates. $\langle r_{TM} \rangle$ emerges as a control parameter that governs the steady state network geometry. Below a critical $\langle r_{TM} \rangle$, which is 0.94 s^{-1} in our simulations, networks geometrically collapse into clusters, while above this critical $\langle r_{TM} \rangle$, they preferentially evolve into ring-like geometries (Fig. 4a and Fig. S6). The radial distribution of the ring state is characterized by higher R_{median} and smaller standard deviation compared with the cluster phase (Fig. 4b). Interestingly, R_{median} as
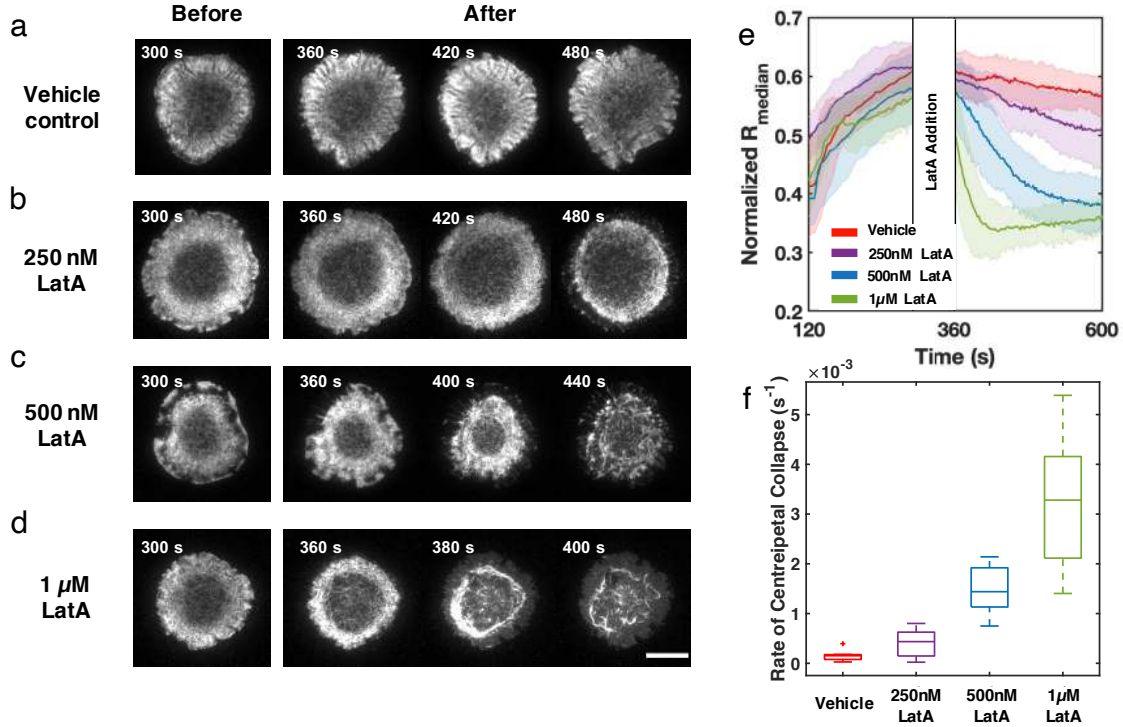
Figure 2: **Inhibition of treadmilling induces collapse of actin rings in live T cells.** (a-d) Timelapse montages of Jurkat T cells expressing F-tractin-EGFP spreading on anti-CD3 coated glass substrates. Cells were treated with (a) vehicle (0.1% DMSO), (b) 250 nM LatA, (c) 500 nM LatA, or (d) 1 μM LatA between 300 and 360 seconds after contact with activating surface. Timelapse images illustrate the centripetal collapse of the actin ring upon treatment with LatA. Timescales of this collapse depend on the concentration of LatA as can be seen from the timestamps on the images. Scale bar is 10 μm. (e) Quantification of the spatial organization of the actin network using the normalized median of radial filament density distribution. Shaded error bars represent the standard deviations across trajectories (7-11 cells per condition). (f) Box plots showing the rate of centripetal collapse, measured as the slope of the R_{median} distribution after inhibition.

a function of $\langle r_{TM} \rangle$ displays a sharp increase from the cluster state to the ring state. We then quantified the network remodeling speed by measuring the slopes of the mean R_{median} trajectories and found that the network remodeling speed is positively associated with $\langle r_{TM} \rangle$ (Fig. 4c), indicating that $\langle r_{TM} \rangle$ is a driving force for network structural evolution.

We next explored the chemical and mechanical properties of actin networks at various tread-
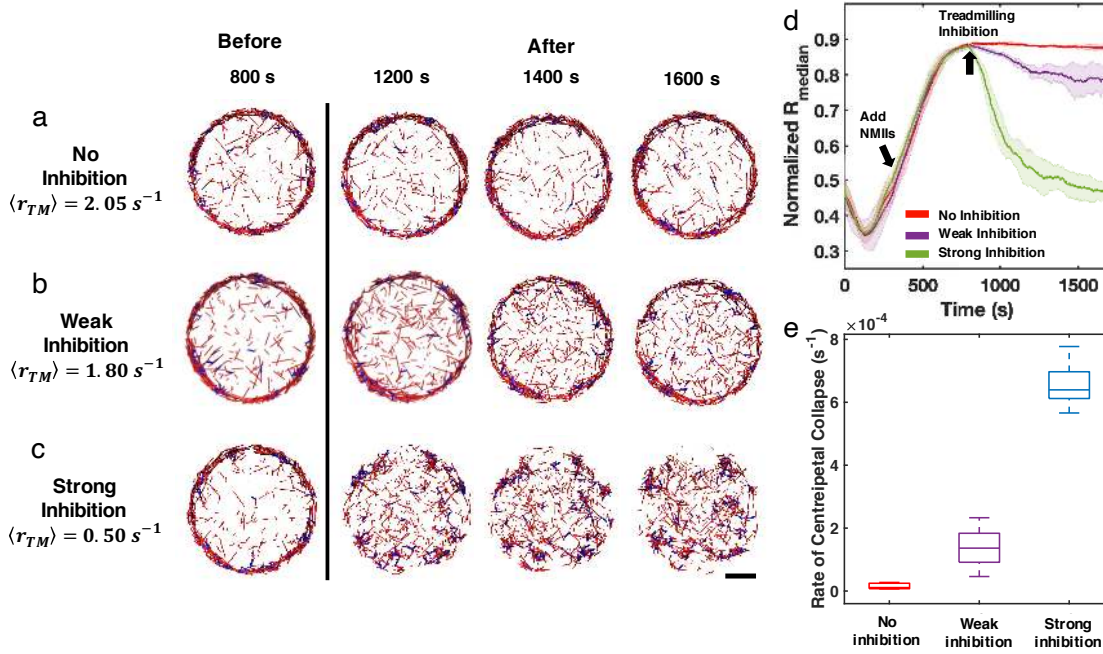
9

Figure 3: **Inhibiting treadmilling in silico recapitulates experimentally observed collapse of actin rings.** Timelapse montages of simulations mimicking treadmilling inhibition for $\langle r_{TM} \rangle$ = $2.05 s^{-1}$ (a), $1.80 s^{-1}$ (b) and $0.50 s^{-1}$ (c). Indicated $\langle r_{TM} \rangle$ is the averaged treadmilling from 1500s to the end of simulations. Scale bar indicates 1 μm. (d) Medians of radial filament density distribution at different treadmilling inhibition condition. (e) Rate of centripetal collapse rate, measured as the slope of the R_{median} distribution after inhibition. (d-e) The shaded color and error bars represents the standard deviation across trajectories, 5 runs per condition.

milling rates. We found that the numbers of F-actin filaments, bound linkers, and bound motors remain nearly constant across different $\langle r_{TM} \rangle$, while distributions of diffusive molecules, such as G-actin and nucleators, also did not show spatial localization, being uniformly distributed throughout the simulation volume (Fig. S7). These observations suggest that ring-like architectures do not form because of the enrichment of soluble constituent molecules near the periphery.

The lack of enrichment of soluble molecules in the periphery suggested a possible energetic origin of the structures. We thus examined the mechanical energy (U_{Mech}) of the system. We found that U_{Mech} is negatively correlated with R_{median}, regardless of the structural state

(Fig. 4d). Since higher R_{median} indicates localization of actin filaments at the network periphery, this negative correlation indicates the configurations with the lowest mechanical energy are those with a ring-like geometry. In our simulations, U_{Mech} primarily arises from filament bending, which decreases with increasing $\langle r_{TM} \rangle$ (Fig. 4e). We found that U_{Mech} undergoes a sharp reduction when $\langle r_{TM} \rangle$ reaches the critical threshold, with U_{Mech} of actin rings being 2-3 fold lower than that of clusters. These results suggest that the peripheral arrangement of actin filaments is more energetically favorable than more distorted configurations found in centripetal clusters.

Detailed mechanochemical modeling using MEDYAN shows that active actin networks exhibit a striking geometric transition upon changes in the filament treadmilling rate. We found that two distinct types of dynamic patterns emerge due to the interplay between treadmilling rates and NMII contractility in an initially disordered network: (1) actin clusters in slow-treadmilling networks and (2) ring-like and cortex-like structures in fast-treadmilling networks. This geometric transition does not require filament tethering to the boundary or a spatially biased filament assembly. We also observed a sharp transition in the system's mechanical energy during the transformation from a multi-cluster network to a ring architecture. Such a sharp change in geometry and mechanical energy, induced by tuning filament treadmilling speed, is indicative of a finite size phase transition.

While phase transitions in many biomolecular systems are often driven by passive biomolecular interactions (*34, 35*), in this work we identified a phase transition in cytoskeletal networks that is induced by non-equilibrium actomyosin dynamics. Our analysis shows that the formation of actin rings and cortices arises from the competition between filament treadmilling and myosin induced contraction. The addition of myosin motors and crosslinkers to an initially disordered actin network induces contractile forces, creating an energy trap that globally attracts actin filaments into clusters (*36*) (Fig. 4f). Rapid filament treadmilling provides a mechanism
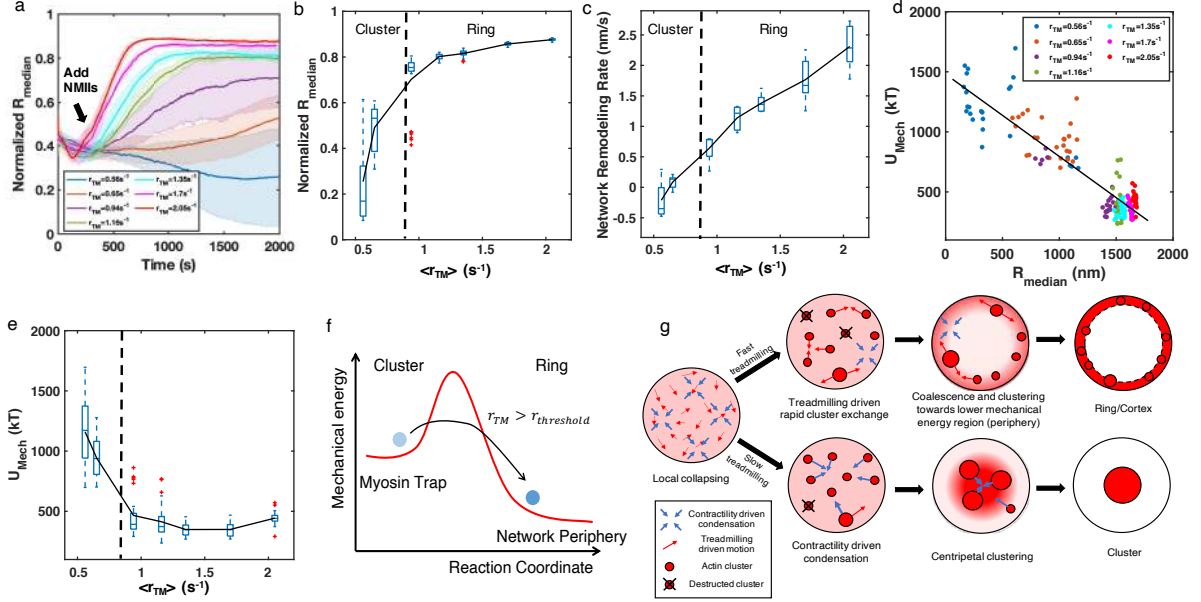
Figure 4: **Energetic origins of actin rings.** (a) Normalized medians of radial filament density distribution (R_{median}) at different $\langle r_{TM} \rangle$ (0.56 s^{-1} to 2.05 s^{-1}) are shown. The shaded colors represent the standard deviation of means for 5 runs. (b) The box plot shows the average R_{median} at the last 500 seconds of simulation at each treadmilling rate. Solid line connects the mean R_{median} at each $\langle r_{TM} \rangle$. (c) The box plot shows the speed of network remodeling, measured as the slope of R_{median} between 300 seconds and steady state. Solid line connects the mean remodeling rates at each $\langle r_{TM} \rangle$. (d) Mechanical energy (U_{Mech}) and the corresponding R_{median} at different $\langle r_{TM} \rangle$. Each data point represents the average U_{Mech} and R_{median} per 100 seconds of the last 500 seconds of simulation (5 runs per condition). U_{Mech} is the sum of the bending energy of actin filaments and the stretching energy of filaments, motors, and linkers. Solid line represents a linear fit of the data. (e) The box plot shows the steady state U_{Mech} at each treadmilling rate (5 runs per condition). Solid line connects the mean U_{Mech} at each $\langle r_{TM} \rangle$. (f) A graphical description showing the envisioned energy landscape for generating actin cortices. (g) Schematic showing the formation of actin ring/cortex *versus* clusters. At low treadmilling rates, networks are dominated by myosin-driven contraction, leading to centripetal collapse into clusters (lower). Faster filament treadmilling allows networks to overcome the myosin-driven centripetal motion, where filaments tend to move to network periphery due to lower energy (upper).

12

for escaping these traps (*21, 26, 37*), creating smaller clusters that rapidly dissolve and reappear. In this state, the network has more freedom to remodel its structure in order to lower the mechanical energy. Indeed, our analysis suggests that as the actin filament distribution shifts to the network periphery, the smaller curvature at the boundary results in a decrease in filament bending, thereby lowering the mechanical energy of the network (Fig. 4d-e). As a consequence, actin filaments at high treadmilling speeds rapidly accumulate at the network periphery, contributing to the build up of an actin ring in flattened volumes or actin cortices in fully 3D spherical geometries (Fig. 4g, higher). In contrast, networks undergoing slow filament treadmilling are trapped in cluster-type configurations that have higher mechanical energy. Such cluster networks are dominated by myosin-driven contractility, leading to a highly non-ergodic state in which actin filaments undergo centripetal collapse (Fig. 4g, lower).

Although some previous computational studies have studied how network morphology and contractility are regulated by treadmilling rates (*23, 37, 38*), active formation of cortical shell-like or ring-like networks and their underlying mechanisms have not been explained before. In this work, we have shown that rapid treadmilling and the presence of myosin are sufficient to create ring-like or cortex-like actomyosin networks in a system with confined boundaries. Furthermore, it is likely that filament binding to cell membrane (*39*) or the spatially biased localization of actin assembly regulators, such as Arp2/3 (*16*), can further enhance their formation. These extensions to the model will be the subject of our future work and will enable us to more precisely elucidate the mechanisms of these complex actomyosin structures in different biological contexts. Studying the building blocks of these structures will bring new mechanistic insights into the organization and dynamics of cortices/rings and their defects, which occur in primary immunodeficiencies, autoimmune disorders, and cancers.

Methods

Simulation setup

In this work, we employed an open-access mechanochemical platform for simulating active matter (MEDYAN (*21*)) to investigate the spatiotemporal evolution of actin networks under different treadmilling and myosin motor conditions. MEDYAN accounts for two overlapping phases and their interactions. 1) Diffusing G-actin and unbound formins, NMII and linkers are spatially dissolved in a solution phase. In this phase, the network is discretized into compartments based on the Kuramoto length of G-actin, which is the mean-free path that G-actin molecules are expected to diffuse before undergoing their next reaction (*40*). Diffusing chemical species are assumed to be well-mixed within each compartment, and inter-compartment transports are modeled as stochastic diffusion reactions. 2) Polymeric filaments and bound species comprise the continuous polymeric phase which is overlaid on the solution phase. The polymeric phase is mechanically active, where filament bending, stretching, and steric interactions are taken into account. Bound motors and linkers are modeled as harmonic springs based on the mechanical properties of NMII and alpha-actinin. A boundary repulsion potential restricts filaments within the volume boundary. Filament polymerization is affected by interactions with the boundary, following the Brownian Ratchet model (*41*). The following chemical reactions stochastically occur among the two phases: filaments can polymerize, depolymerize, and interact with myosin and crosslinker; formins are able to bind to G-actin and nucleate filaments; filaments that are only two monomers long can be rapidly destroyed. The chemical reaction modeling engine is based on an efficient and statistically accurate Next Reaction Method (NRM) (*42*), which is a variant of the Gillespie Algorithm (*43*).

We initialized *de novo* cytoskeletal networks in MEDYAN with small seed filaments, 40 μM diffusing G-actin, and 100 nM filament nucleators based on their reported cytoplasmic con-

centrations (*44*). Most of the simulations were carried out in a thin oblate geometry, having a diameter ranging from 3.8 μm to 10 μm and an effective height of 200 nm. The spherical simulation volume has a diameter of 4 μm. We tuned the barbed end polymerization rate and pointed end depolymerization rate to model the effects of treadmilling promoters such as formin, profilin, and cofilin (see SI-2). To monitor the actual speed of treadmilling, we define $\langle r_{TM} \rangle$ as the average barbed end elongation rate, which is also equal to the shortening rate of the pointed end at steady state. Networks were allowed to assemble with only filament polymerization, depolymerization, nucleation, and disassembly for 300 seconds. At 300 s, 0.06 μM NMII and 4 μM alpha-actinin crosslinkers are added. The local density of clusters and rings were measured using a customized density based clustering algorithm. Further simulation details can be found in SI-1.

Cell culture and transfection

E6.1 Jurkat T cells were grown in RPMI medium supplemented with 10% Fetal Bovine Serum (FBS) and 1% penicillin-streptomycin at 37°C in a CO_2 incubator. Transfections were performed with 2×10^5 cells using 1 μg of plasmid by electroporation using a Neon electroporation kit (Thermo Fisher Scientific). Prior to imaging, cells were transferred to CO_2 independent L-15 medium (Fisher Scientific).

Plasmids and reagents

pEGFP-C1 F-tractin-EGFP was a gift from Dyche Mullins (Addgene plasmid # 58473; http://n2t.net/addgene:58473; RRID:Addgene_58473) (*45*). Latrunculin A was purchased from Sigma Aldrich and its solvent, dimethyl sulfoxide (DMSO) was purchased from Thermo Fisher Scientific.

Preparation of glass coverslips

Sterile 8-well chambers (Cellvis) were incubated with 0.01% poly-L-lysine solution in distilled water for 10 minutes and then dried at 37°C for 1 hour. Poly-L-lysine coated chambers were then incubated with anti-human CD3 antibody (HIT3a clone, Thermo Fisher Scientific) in PBS at a concentration of 1 μg/mL for 2 hours at 37°C or overnight at 4°C. Following incubation, the chambers were washed 5 times with L-15 and warmed prior to imaging.

Microscopy

Transfected T cells were seeded on anti-CD3 coated glass coverslips and allowed to activate for 5 minutes. Chambers were maintained at 37°C using a stage-top incubator (Okolab). Latrunculin A or vehicle (DMSO) were added at specified concentrations 5 minutes after seeding the cells. Fluorescence and interference reflection microscopy (IRM) images were acquired using an inverted microscope (Ti-E, Nikon, Melville, NY) with a scientific CMOS camera (Prime BSI, Photometrics, Tucson, AZ) with a frame interval of 2 seconds. F-tractin-EGFP was imaged using total internal reflection fluorescence (TIRF), using a 60X, 1.49 NA oil immersion objective. One background image was captured during every session in order to perform background subtraction.

Image analysis

Initial preprocessing of images was done using Fiji (*46*). A custom MATLAB script was written to perform background subtraction. The IRM images were used to find the outline and centroid of the cells. 50 uniformly spaced lines were drawn from the centroid and these 50 line profiles were pooled together to generate a histogram of intensities as a function of a normalized distance to the centroid. The median of the distribution of intensities (and hence F-actin) was estimated for each time point.

References

1. G. Salbreux, G. Charras, E. Paluch, *Trends in Cell Biology* **22**, 536 (2012).

2. L. Blanchoin, R. Boujemaa-Paterski, C. Sykes, J. Plastino, *Physiological Reviews* **94**, 235 (2014).

3. M. P. Stewart, *et al.*, *Nature* **469**, 226 (2011).

4. M. Bovellan, *et al.*, *Current Biology* **24**, 1628 (2014).

5. R. Levayer, T. Lecuit, *Trends in Cell Biology* **22**, 61 (2012).

6. M. Fritzsche, C. Erlenka mper, E. Moeendarbary, G. Charras, K. Kruse, *Science Advances* **2**, e1501337 (2016).

7. B. Bugyi, M.-F. Carlier, *Annual review of biophysics* **39**, 449 (2010).

8. T. D. Pollard, *Annu Rev Biophys Biomol Struct* **36**, 451 (2007).

9. Q. Ni, G. A. Papoian, *Cytoskeleton* **76**, 562 (2019).

10. T. H. Tan, *et al.*, *Science Advances* **4**, 1 (2018).

11. M. Bergert, S. D. Chandradoss, R. a. Desai, E. Paluch, *Proceedings of the National Academy of Sciences of the United States of America* **109**, 14434 (2012).

12. K. L. Hui, A. Upadhyaya, *Proceedings of the National Academy of Sciences of the United States of America* **114**, E4175 (2017).

13. J. Yi, X. S. Wu, T. Crites, J. A. Hammer, *Molecular Biology of the Cell* **23**, 834 (2012).

14. A. Babich, *et al.*, *Journal of Cell Biology* **197**, 775 (2012).

15. J. A. Hammer, J. Wang, M. Saeed, A. Pedrosa, *Annual Review of Immunology* **37**, 201 (2018).

16. S. Murugesan, *et al.*, *The Journal of cell biology* **215**, 383 (2016).

17. O. Collin, *et al.*, *Current Biology* **18**, 1288 (2008).

18. K. Xu, G. Zhong, X. Zhuang, *Science* **339**, 452 (2013).

19. M. P. Murrell, M. L. Gardel, *Proceedings of the National Academy of Sciences of the United States of America* **109**, 20820 (2012).

20. I. Linsmeier, *et al.*, *Nature Communications* **7**, 12615 (2016).

21. K. Popov, J. Komianos, G. A. Papoian, *PLOS Computational Biology* **12**, 1 (2016).

22. J. Li, T. Biel, P. Lomada, Q. Yu, T. Kim, *Soft Matter* **13**, 3213 (2017).

23. M. Mak, M. H. Zaman, R. D. Kamm, T. Kim, *Nature Communications* **7**, 10323 (2016).

24. D. R. Kovar, E. S. Harris, R. Mahaffy, H. N. Higgs, T. D. Pollard, *Cell* **124**, 423 (2006).

25. M. Malik-garbi, *et al.*, *Nature Physics* **15**, 509 (2019).

26. P. M. McCall, F. C. MacKintosh, D. R. Kovar, M. L. Gardel, *Proceedings of the National Academy of Sciences of the United States of America* **116**, 12629 (2019).

27. S. Jansen, *et al.*, *Nature Communications* **6**, 7202 (2015).

28. A.-C. Reymann, *et al.*, *Molecular Biology of the Cell* **22**, 2541 (2011).

29. I. Fujiwara, D. Vavylonis, T. D. Pollard, *Proceedings of the National Academy of Sciences of the United States of America* **104**, 8827 (2007).

30. I. Fujiwara, M. E. Zweifel, N. Courtemanche, T. D. Pollard, *Current Biology* **28**, 3183 (2018).

31. M. Pring, M. Evangelista, C. Boone, C. Yang, S. H. Zigmond, *Biochemistry* **42**, 486 (2003).

32. H. F. Lodish, *Molecular cell biology* (W.H. Freeman, 2000).

33. E. G. Yarmola, *Journal of Biological Chemistry* **275**, 28120 (2000).

34. P. Li, *et al.*, *Nature* **483**, 336 (2012).

35. C. P. Brangwynne, *et al.*, *Science* **324**, 1729 (2009).

36. J. E. Komianos, G. A. Papoian, *Physical Review X* **8**, 21006 (2018).

37. T. Kim, M. L. Gardel, E. D. Munro, *Biophysical Journal* **106**, 526 (2014).

38. D. B. Oelz, B. Y. Rubinstein, A. Mogilner, *Biophysical Journal* **109**, 1818 (2015).

39. T. Litschel, *et al.*, *Nature Communications* **12**, 1 (2021).

40. L. Hu, G. A. Papoian, *Biophysical Journal* **98**, 1375 (2010).

41. C. S. Peskin, G. M. Odell, G. F. Oster, *Biophysical Journal* **65**, 316 (1993).

42. M. A. Gibson, J. Bruck, *The Journal of Physical Chemistry A* **104**, 1876 (2000).

43. D. T. Gillespie, *Journal of Physical Chemistry* **81**, 2340 (1977).

44. J.-Q. J.-Q. Wu, T. D. Pollard, *Science* **310**, 310 (2005).

45. B. J. Belin, L. M. Goins, R. D. Mullins, *BioArchitecture* **4**, 189 (2014).

46. J. Schindelin, *et al.*, *Nature methods* **9**, 676 (2012).

Acknowledgments

Supplementary materials

Supplementary Text

Figs. S1 to S7

Videos. 1-10

Supplementary Files

This is a list of supplementary files associated with this preprint. Click to download.

- Video1.mp4
- Video2.mp4
- Video3.mp4
- Video4.mp4
- Video5.mp4
- Video6.mp4
- Video7L15.avi
- Video8DMSO.avi
- Video9250nMLatA.avi
- Video10500nMLatA.avi
- Video111uMLatA.avi
- SI.pdf